Available online at www.sciencedirect.com
ScienceDirect
Trans. Nonferrous Met. Soc. China 35(2025) 4007−4020
Transactions of Nonferrous Metals Society of China
www.tnmsc.cn

Effect of aging treatment on bending collapse and energy absorption of 7003 aluminum alloy bumper beams

Cong-chang XU[1,2], Han-lin XIANG[1,2], Teng ZHAN[1,2], Peng-cheng GUO[2], Luo-xing LI[1,2]

1. College of Mechanical and Vehicle Engineering, Hunan University, Changsha 410082, China;
2. Research Institute of Hunan University in Chongqing, Hunan University, Chongqing 400044, China

Received 26 March 2024; accepted 24 March 2025

Abstract: The bending collapse and energy absorption of 7003 aluminum alloy bumper beams under four aging conditions (pre-aging, under-aging, peak-aging, and over-aging) were investigated through three-point bending tests. Microstructural characterization was performed using scanning electron microscopy and transmission electron microscopy. Based on the Swift−Hockett−Sherby constitutive model combined with the Gurson−Tvergaard−Needleman damage model, the plastic response and fracture behavior of the 7003 aluminum alloy under uniaxial tension and three-point bending were accurately predicted. The results showed that the peak bending force of the beams was proportional to the strength under different aging states, while stress triaxiality governed the cracking failure. Pre-aged and under-aged beams resisted cracking until reaching 250 mm displacement due to stress transition from tensile to compression on the bottom surface. The under-aged beam exhibited optimal energy absorption (7.86 kJ) and a higher peak force (38.75 kN).

Key words: 7003 aluminum alloy beam; aging treatment; three-point bending test; bending collapse; energy absorption

1 Introduction

The bumper is an important component of the passive safety system in a vehicle, playing a major role in receiving impact force and absorbing energy through its deformation [1]. Compared to traditional internal combustion engine vehicles, new energy vehicles exhibit an over 10% increase in total mass, necessitating enhanced crashworthiness of the vehicle body to meet stringent collision safety requirements [2]. Consequently, the development of cost-effective, high-performance bumpers has become a primary design objective for automotive engineers [3].

The assessment of bumper crashworthiness predominantly relies on the established testing standards, which include pendulum impact, full-width barrier impact, and 40% offset barrier impact tests. Notably, the dimensions of both the pendulum and the barrier align closely with those of the bumper beam, thereby ensuring that these tests can effectively replicate real-world vehicle collision scenarios [4]. In addition to the full frontal bumper collision, the most common accidents are column collisions that impact vertical hard objects (such as telephone poles or trees). In column collision, the deformation of the bumper is concentrated on the local bumper beam, and the energy absorption box cannot completely collapse and absorb energy, resulting in more serious damage to the bumper beam [5]. So, the automobile designers put forward higher requirements for the bending energy absorption of bumper beams. BAI et al [6] investigated the three-point bending collapse of the dual rectangle thin-walled tube using theoretical

Corresponding author: Luo-xing LI, Tel: +86-13786199121, E-mail: luoxing_li@hnu.edu.cn
https://doi.org/10.1016/S1003-6326(25)66926-3

prediction and experimental verification. The global energy equilibrium theory was applied to deriving the bending characteristic of the dual rectangle thin-walled tube. KIM and REID [7] presented a self-consistent method to predict the response of the bending moment for the empty tube. QIAN et al [8] carried out a comprehensive experimental/numerical study on a 6060 T6 bumper profile subjected to combined shear-compression load.

Aluminum alloys are ideal materials for the bumper beam, due to their good formability, high specific strength, and high recycling value [9,10]. In particular, aluminum extrusions with the complicated cross-sectional shapes and flexible wall thickness distributions are being increasingly applied to automotive components. Therefore, most of the present beams are made of aluminum alloys. SUN et al [11] developed the multi-objective optimization for the wall thicknesses of aluminum alloy bumper under different low-speed impacting conditions. BILSTON et al [12] conducted a parametric study of the cross-section shape of aluminum tubes in dynamic three-point bending. DU et al [13] constructed a theoretical prediction model to reveal the bending collapse mechanism of single-box multi-cell section aluminum alloy bumper beams under three-point bending, and derived the theoretical prediction model of bending energy. HUANG et al [14] explored the effects of load and boundary conditions on the transverse bending responses of 6063 aluminum square tubes by three-point bending tests, and the finite element model was used to optimize the cross-section parameters of the square tube. WANG et al [15,16] investigated the bending resistance of multi-cell square tubes under three-point bending and employed two methods of dimensionless analysis method and energy analysis method to derive the bending moment response of tubes. With the urgent need for electric vehicles, the addition of battery mass makes electric vehicles 10% heavier than fuel vehicles. Automotive designers have to put forward higher requirements for the bending performance and energy absorption of the bumper beam. RAO et al [17] analyzed the crashworthiness of bumpers made with different materials and thicknesses. The results showed that the materials with high yield strength are best suitable for the manufacturing of bumper beams. Compared with the traditional 6xxx series aluminum alloys, 7xxx series aluminum alloys have a higher specific strength and better mass reduction effect, which gradually attract the attention of designers [18,19].

Aging treatment is an effective way to improve the strength of aluminum alloys, but usually sacrifices their ductility [20]. In this study, without increasing manufacturing costs, the optimized two-stage aging heat treatment process not only ensures the strength and toughness of the aluminum alloy material but also achieves the high-performance requirements for three-point bending of crash beams. By investigating the influence of aging treatment on the mechanical properties and fracture elongation of 7003 aluminum alloy beams, and analyzing the bending collapse and energy absorption characteristics under various aging conditions, this research ultimately provides both technical support and theoretical guidance for the fabrication of high-performance bumper crash beams.

2 Experimental

2.1 Materials

An industrial 7003 aluminum alloy beam was used in this study. The measured chemical composition of the beam was illustrated in Table 1. The thickness of the beam was 3 mm, its extrusion ratio was 16.5, its extrusion die temperature was 470 °C, the casting rod temperature was 490 °C, and the temperature of the extrusion outlet was constrained between 510 and 530 °C. The materials received in the online extrusion quenched state were subjected to natural aging (NA) at room temperature (RT) for 3 d, followed by two-stage artificial aging (AA) treatments setting as ((105 °C, 6 h) + (150 °C, 0−20 h)) (see Fig. 1). The process parameters of aging treatments were illustrated in Table 2.

2.2 Uniaxial tensile tests

Uniaxial tensile tests along the extrusion direction of the 7003 aluminum alloy beams were

Table 1 Measured chemical composition of 7003 aluminum alloy beam (wt.%)

Zn	Mg	Zr	Cu	Si
5.71	0.87	0.086	0.015	0.032
Fe	Mn	Cr	Ti	Al
0.11	0.002	0.001	0.022	Bal.

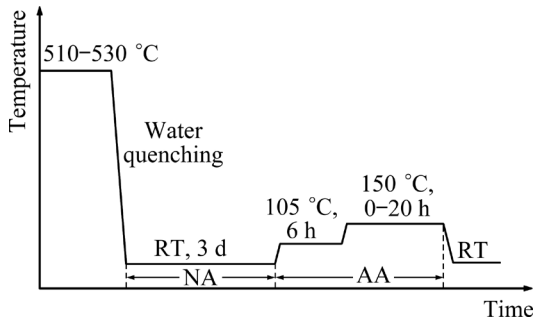

Fig. 1 Schematic diagram of two-stage aging treatments

Table 2 Process parameters of aging treatments applied to beams

Sample	Aging treatment parameter
Pre-aged	105 °C, 6 h
Under-aged	(105 °C, 6 h) + (150 °C, 4 h)
Peak-aged	(105 °C, 6 h) + (150 °C, 8 h)
Over-aged	(105 °C, 6 h) + (150 °C, 20 h)

conducted using an MTS−809 axial tensile testing machine at room temperature with a tensile speed of 3 mm/min. Figure 2 illustrates the dimensions of the tensile specimen following ASTM E8M-04. The test under the same conditions was repeated at least three times, and the three tests with a deviation within the range of ±5% were taken as effective test. Yield strength, ultimate tensile strength and elongation were the averages of three valid experiments. Digital image correlation (DIC) technique was used to measure the strain components, within the gauge area distribution of specimens. The morphology of the fracture surface of the tensile specimen was observed using an FEI Helios G3 instrument. All fracture photographs were taken from the center of the fracture surface.

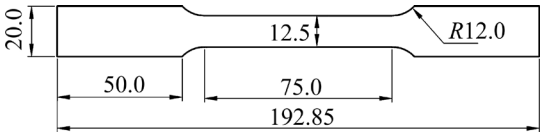

Fig. 2 Dimensions of tensile specimen (Unit: mm)

2.3 Microstructure characterization

The TEM examination was conducted using an FEI Tecnai F20 transmission electron microscope operating at 200 kV in a vacuum environment. Disk specimens with 3 mm in diameter were punched out directly from slices, and then mechanically ground to 100 μm in thickness. The disk specimens were electro-polished using an electrolytic dual spray equipment with solution of 30 vol.% HNO_3 and 70 vol.% methanol at 18 V in the temperature range from −30 to −25 °C.

2.4 Three-point bending tests

The cross-sectional dimensions of the beam specimens are provided in Fig. 3(a). Quasi-static three-point bending tests were conducted using an Instron 8802 material test system. As shown in Fig. 3(b), each beam was simply supported on two fixed cylindrical rollers with a radius of 17 mm, giving a support span of 920 mm. A cylindrical punch with a radius of 127 mm was used to apply the load at the mid-span at a constant velocity of 50 mm/min. In accordance with the design requirements for the bumper beam, the punch displacement was limited to a maximum of 250 mm. The experiments focused on evaluating the bearing capacity, collapse behavior, and energy absorption of the beams under three-point bending.

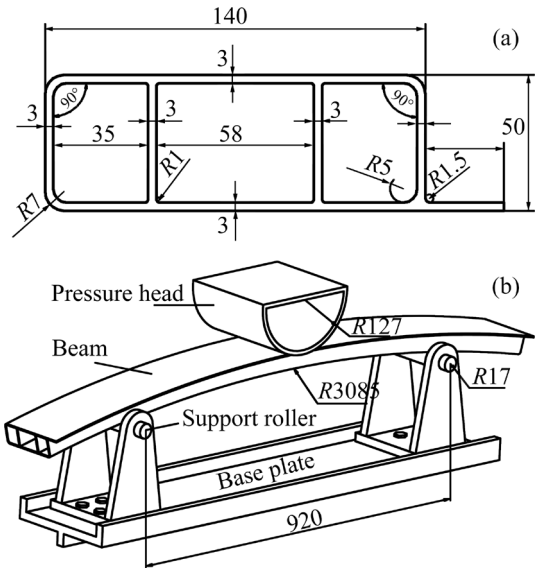

Fig. 3 Schematic diagrams of beam cross-sectional dimensions (a) and load condition of three-point bending test (b) (Unit: mm)

3 Results and discussion

3.1 Mechanical properties

3.1.1 Tensile properties

The tensile properties of 7003 aluminum alloy beams during the first-stage aging at 105 °C for 6 h and the second-stage aging at 150 °C for 0−20 h are shown in Fig. 4. The ultimate tensile strength (UTS)

and yield strength (YS) are observed to increase linearly during the first-stage aging. Following that, the strength increases quickly with the increase of the aging time. However, the rate of increase in strength slows down at 4 h of the second-stage aging. At this point, UTS and YS reach 344 and 303 MPa, respectively. As the aging continues, the strength gradually increases to a plateau with a peak value at 8 h. The UTS, YS and elongation (EL) are 356 MPa, 327 MPa and 16.5%, respectively. After the plateau, a slight decrease in strength is observed. During the entire aging treatment, the EL continues to decrease with increasing the aging time. The engineering stress−strain curves of the four typical aging treatments: 105 °C, 6 h (pre-aging), (105 °C, 6 h) + (150 °C, 4 h) (under-aging), (105 °C, 6 h) + (150 °C, 8 h) (peak-aging) and (105 °C, 6 h) + (150 °C, 20 h) (over-aging) were selected for the comparative analysis, as depicted in Fig. 4(b). The strain hardening rate of the 7003 aluminum alloy beams is observed to decrease gradually as the aging treatment continues.

The strengthening mechanisms of 7xxx series aluminum alloys mainly include solid solution strengthening, grain boundary strengthening and precipitation strengthening [21]. Precipitation strengthening is the most effective strengthening mechanism. The type, size and quantity of precipitates affect the strength of materials greatly [22−24]. When the size of precipitates is relatively small, i.e., precipitates are primarily composed of fine GP zones and η' phases, dislocation cuts through the fine precipitates. Therefore, the strengthening effect ($\Delta\tau_p$) can be expressed as follows [25]:

$$\Delta\tau_p = \alpha f^{1/2} r^{1/2} \quad (1)$$

where α is a constant, f is the volume fraction of precipitates, and r is the radius of precipitates.

Figure 5 depicts the TEM morphologies of precipitates in the 7003 aluminum alloys under different aging treatments. The corresponding selected area electron diffraction (SAED) patterns are also shown in Fig. 5. The SAED images verify that all images are obtained in the direction along the ⟨112⟩ zone axis of the Al matrix. The figures indicate that the precipitates in the alloy matrix after pre-aging are fine and diffused, with elliptic and disk-like morphology of approximately 2 nm in diameter and 4−6 atomic layers in thickness. The fast Fourier transform (FFT) diagram of the ⟨112⟩Al projection direction reveals that diffraction spots are observed on the 1/2{311}Al crystal plane, considered to be GP II zones [26]. In addition, some bright diffraction spots (circular marks) are observed in 1/2{220}Al, not corresponding to the GP zone and the η' phase, but to the Al_3Zr phase [27]. Pre-aging treatment produces a large number of dispersed GP II zones in the matrix (Fig. 5(a)). Additional resistance is generated when dislocation passes through the GP II zones during deformation, thus increasing the bearing capacity [25]. The YS and UTS increase from the initial 183 and 269 MPa to 225 and 309 MPa, respectively. Figure 5(b) depicts diffuse scattering fringes along the direction of ⟨111⟩Al, and no diffraction spots of η' phase are observed. So, GP II zones are identified to be the primary precipitated phase of the alloy after under-aging treatment. As the aging time increases, both the volume fraction and radius of GP II zones increase sharply, and the strength of the alloy is further improved. After under-aging treatment, the thickness and diameter of GP II zones reach 1 and 3.5 nm, respectively. The YS and UTS reach 303 and 344 MPa, respectively.

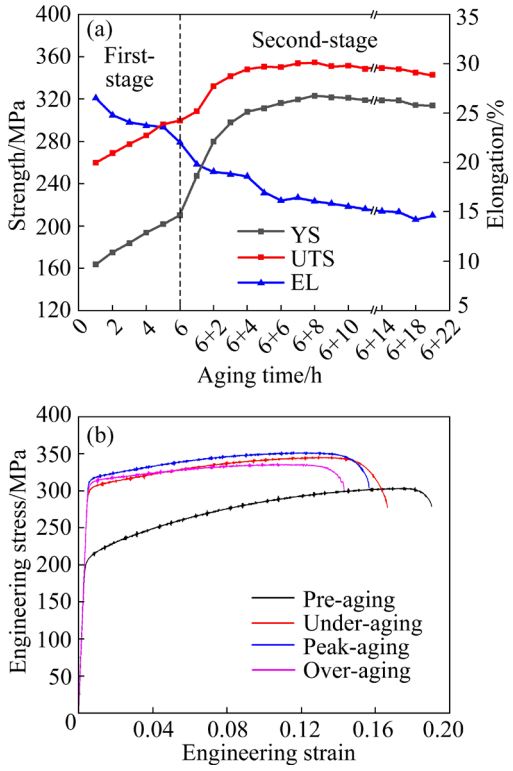

Fig. 4 Tensile properties of 7003 aluminum alloy beams under different aging treatments: (a) YS, UTS and EL; (b) Engineering stress−strain curves

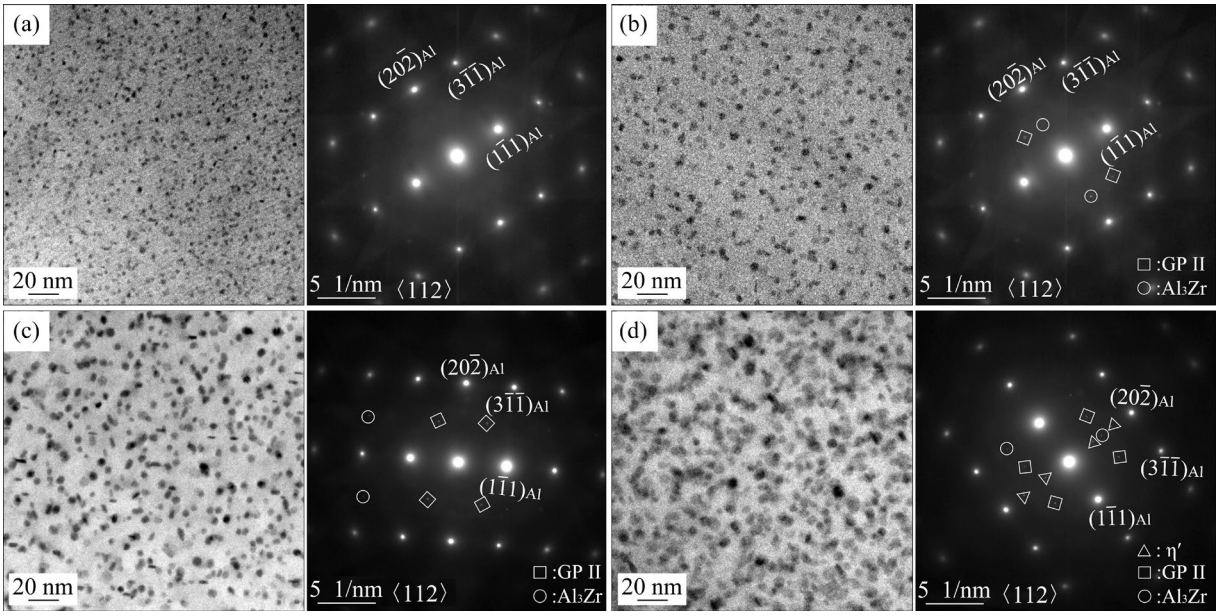

Fig. 5 TEM and SADP images of precipitates in 7073 aluminum alloy under different aging treatments: (a) Pre-aging; (b) Under-aging; (c) Peak-aging; (d) Over-aging

When the size of precipitates is relatively large, i.e., precipitates are primarily composed of coarse η phases, they are difficult to cut through during the deformation process. In this case, the strengthening mechanism is changed to the Orowan bypass mechanism, which can be expressed as follows [28]:

$$\Delta\tau_{\mathrm{p}}=\beta f^{1/2}r^{-1} \tag{2}$$

where β is a constant.

Therefore, the strength of 7003 aluminum alloys is positively correlated with the radius and volume fraction of the precipitates with small size. However, when the precipitates are too large to be cut through by dislocations, the strength of alloys is negatively correlated with the radius of the precipitates, but still positively related to their volume fraction. As is evident from Fig. 4(a), when the second-stage aging time exceeds 4 h, the increase rate in strength decreases significantly, due to the competition between the strengthening effect induced by the increase in the volume fraction and the weakening effect induced by the increase in the precipitate size. When the peak-aging is attained, the precipitates in the matrix are obviously coarsened (see Fig. 5(c)). Some of the precipitates are rod-shaped, and the other proportion is disc-shaped, indicating that a proportion of GP II zones evolve into η' phases. The thickness and diameter of η' phases are 1.2 and 5 nm, respectively. The YS and UTS reach peak values of 326 and 357 MPa, respectively. During the over-aging, the GP II zones have transformed into η' phases (Fig. 5(d)). The increase rate of the precipitate volume fraction slows down with the increase of aging time. The strength of the alloys decreases gradually as the adjacent precipitates merge and coarsen. As shown in Fig. 5(d), when the second-stage aging duration reaches 20 h, the diameter of the precipitates increases to approximately 7 nm and their thickness is about 1.5 nm. The YS and UTS decrease to 319 and 344 MPa, respectively.

3.1.2 Fracture strain

Figure 6 illustrates the force/von Mises strain−displacement curves of samples during the uniaxial tensile tests. During the uniform plastic deformation stage, the force and von Mises strain increase almost linearly with the increase of loading displacement. Once the necking instability develops, the force drops rapidly and the strain rises sharply.

The pre-aged condition yields the alloy with the highest deformability, demonstrating an unstable strain of 0.148, as shown in Fig. 6(a). As aging time increases, uniform strain gradually decreases, and the lowest unstable strain (0.105) occurs under over-aging conditions, as shown in Fig. 6(d). A similar trend is observed for fracture strain: the pre-aged alloy exhibits the maximum

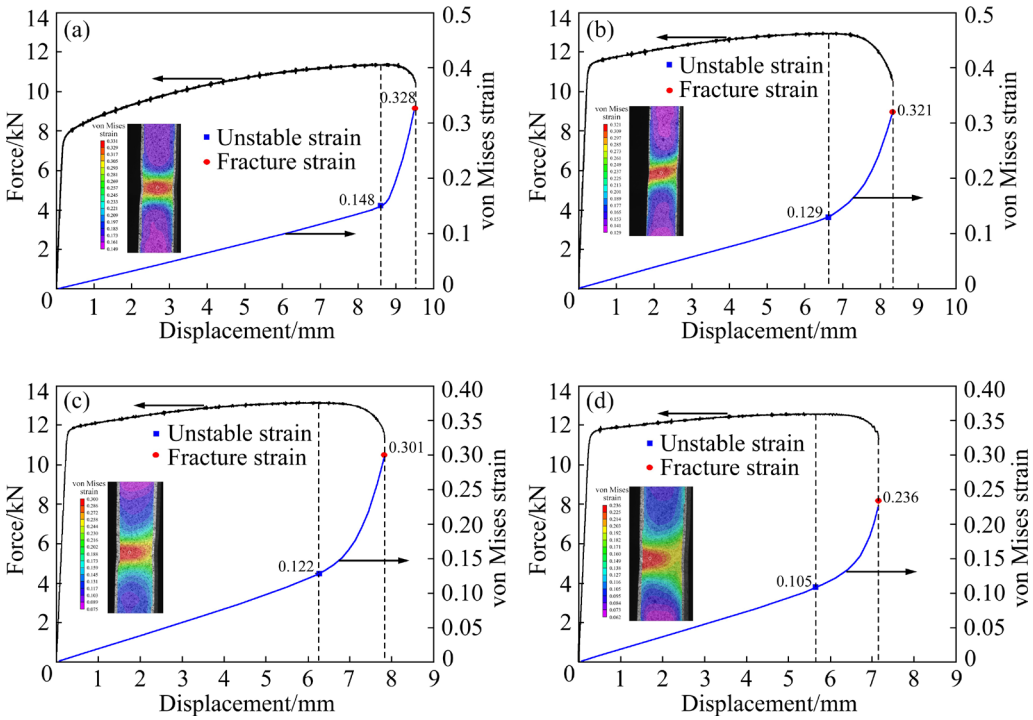

Fig. 6 Force/von Mises strain−displacement curves of tensile samples under different aging treatments: (a) Pre-aging; (b) Under-aging; (c) Peak-aging; (d) Over-aging

value of 0.328, while the over-aged alloy shows the minimum of 0.236, as shown in Figs. 6(a, d). Additionally, the non-uniform strain (post-instability) decreases progressively with longer aging time.

Following pre-aging treatment, a large number of GP II zones are generated in the matrix. The relationships between GP II zones and the Al matrix are fully coherent, indicating that the mismatch strain accounts for only about 4% of the aggregate [21]. At this time, the interaction mechanism between the dislocation and GP II zone is primarily shear, making dislocation accumulation difficult. So the material exhibits high toughness, and fracture strain is the highest under pre-aging treatment. With the addition of high-temperature aging at 150 °C for 4 h, the volume fraction and size of GP II zones gradually increase, leading to a decrease in the fracture strain from 0.328 to 0.321, as shown in Fig. 6(b). Under peak-aging treatment, a proportion of GP II zones transform into η' phase, which is semi-coherent with the matrix. Subsequently, the mismatch strain between the η' phase and the matrix increases, and dislocation tends to entangle and accumulate around the large-sized η' phases, leading to the formation of micro-cracks. After over-aging treatment, η' phase accounts for the majority of precipitates in the matrix with a high mismatch, and dislocation accumulation is significantly higher [29]. Thus, the toughness of the alloy is further reduced; the fracture strain is observed to be 0.236, as shown in Fig. 6(d).

The fracture morphologies of 7003 aluminum alloys after the tensile tests are illustrated in Fig. 7. Under the four aging treatments, the fracture surface of the samples exhibits several dimples, indicating ductile fracture characteristics. Fracture characteristics of 7003 aluminum alloy after the pre-aging treatment (Fig. 7(a)) are similar to those after the under-aging treatment (Fig. 7(b)). The fracture surface is primarily composed of a few large dimples and high-density small dimples. When the peak-aging is attained, the size of dimples in the fracture morphology increases significantly, and coarse precipitates are observed in the center of the dimples (Fig. 7(c)). The coarse precipitates induce crack propagation and reduce the toughness of the alloy. Due to the further coarsening of precipitates, a large number of cleavage planes induced by intergranular fracture can be observed on the fracture surface of the over-aged material (Fig. 7(d)). In conclusion, as the aging time increases,

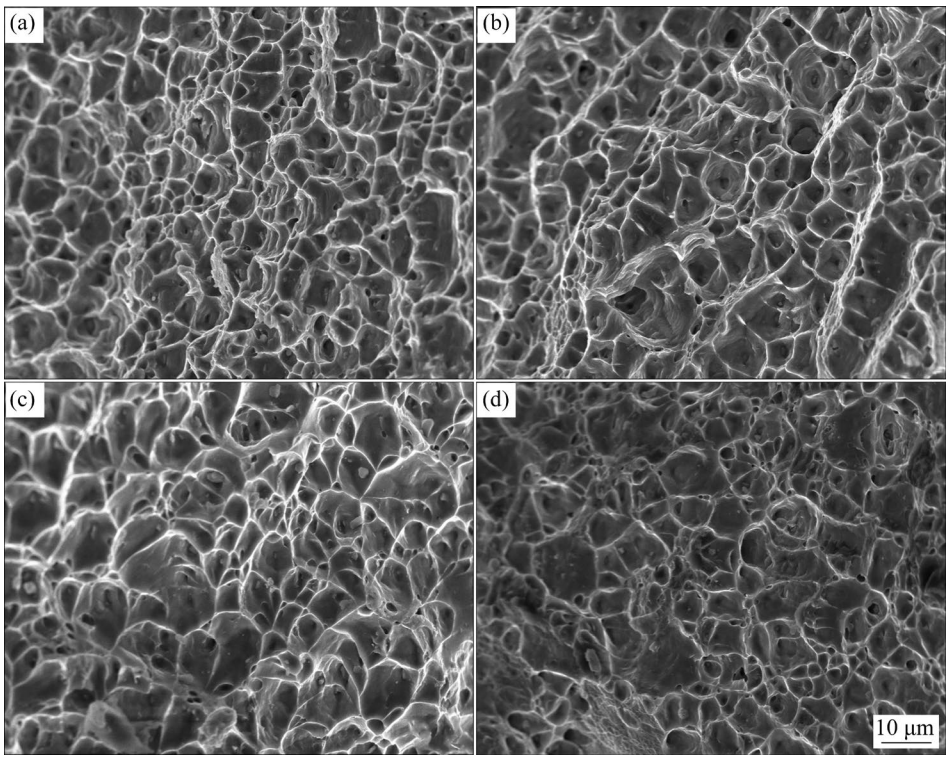

Fig. 7 Fracture morphologies of 7073 aluminum alloy after tensile tests under different aging treatments: (a) Pre-aging; (b) Under-aging; (c) Peak-aging; (d) Over-aging

the strength gap between intragranular and grain-boundary zones increases and the uniform deformation ability of alloys decreases, leading to the reduction of toughness [30].

3.2 Constitutive equation and damage model

3.2.1 Constitutive equation

In order to analyze the bending capacity and fracture behavior of the beams under three-point bending, the stress−strain curves of 7003 aluminum alloy beams are fitted using the Swift−Hockett−Sherby (SHS) constitutive equation as follows [31]:

$$\sigma_{\mathrm{T}}=(1-\alpha)C(\varepsilon_{\mathrm{p}}+\varepsilon_0)^m+ \alpha[\sigma_{\mathrm{sat}}-(\sigma_{\mathrm{sat}}-\sigma_{\mathrm{i}})\exp(-a\varepsilon_{\mathrm{p}}^q)] \quad (3)$$

where σ_{T} is the true stress; α is the weight coefficient; ε_{p} is the plastic strain; C, ε_0 and m are the undetermined fitting constants of the Swift model; σ_{sat}, σ_{i}, a and q are the undetermined fitting constants of the HockettS−herby model.

Matlab software was used to fit and evaluate the seven undetermined coefficients. In order to reversely calibrate the weight coefficient in the material hardening criterion, the finite element (FE) model of the uniaxial tensile test is established (Fig. 8). Hexahedral solid element with the size of 0.75 mm was applied in the FE model. The total number of elements in the FE model is 8200. LS-DYNA explicit algorithm [32] was used for the simulation. The weight coefficients are obtained using simulation and experimental reverse calibration. The parameters in SHS constitutive equation of 7003 aluminum alloys under different aging treatments are listed in Table 3. The true stress−plastic strain curves of 7003 aluminum alloys under different aging treatments fitted by the SHS constitutive equation are shown in Fig. 9.

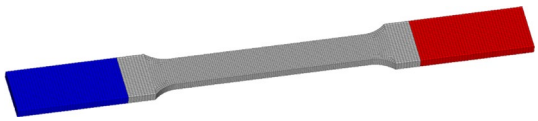

Fig. 8 FE model of uniaxial tensile test

3.2.2 Damage model

The Gurson−Tvergaard−Needlemen (GTN) damage model was used to predict the large deformation and fracture of materials in the tensile tests [33−35]. LI et al [36] investigated the ductile fracture of 6061 Al alloy (T6) using the continuum damage mechanics (CDM)-based Lemaitre model and the GTN damage model, a better ductile fracture

Table 3 SHS constitutive equation parameters of 7003 aluminum alloys under different aging treatments

Aging treatment	C/MPa	ε_0	m	α	σ_{sat}/MPa	σ_i/MPa	a	q
Pre-aging	629.1	0.0414	0.342	0.9	475.6	211.7	4.6	0.927
Under-aging	564.6	0.05	0.207	0.75	464.7	307.5	7.4	1.06
Peak-aging	559.4	0.05	0.19	0.75	452.6	319.4	9.08	1.07
Over-aging	504.4	0.05	0.16	0.95	442.8	314.8	6.83	1.04

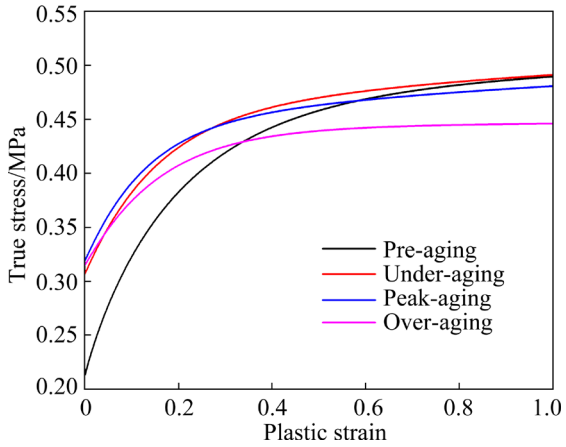

Fig. 9 True stress−plastic strain curves of 7003 aluminum alloys fitted by SHS constitutive equation

prediction was captured by GTN damage model. The Gurson flow function (Φ) is defined as

$$\Phi=\frac{\sigma_M^2}{\sigma_Y^2}+2q_1f^*\cosh\left(\frac{3q_2\sigma_H}{2\sigma_Y}\right)-1-\left(q_1f^*\right)^2=0 \quad (4)$$

where σ_M is the equivalent von Mises stress, σ_Y is the yield stress, σ_H is the mean hydrostatic stress, q_1 and q_2 are the Gurson flow function parameters, and f^* is the effective void volume fraction. The f^* is defined as

$$f^*(f)=\begin{cases}f, f\le f_c\\ f_c+\dfrac{1/q_1-f_c}{f_F-f_c}(f-f_c), f>f_c\end{cases} \quad (5)$$

where f is the void volume fraction, f_c is the critical void volume fraction, and f_F is the void volume fraction in the fracture. The growth of void volume fraction ($\dot{f}$) includes two parts: void nucleation ($\dot{f}_N$) and void growth ($\dot{f}_G$). The formula is defined as

$$\dot{f}=\dot{f}_G+\dot{f}_N \quad (6)$$

It is assumed that the plastically deformed matrix material is incompressible. The growth of existing voids is defined as

$$\dot{f}_G=(1-f_0)\dot{\varepsilon}_{kk}^p \quad (7)$$

where f_0 is the initial void volume fraction, and $\dot{\varepsilon}_{kk}^p$ is the macroscopic plastic volumetric expansion rate. The nucleation of new voids is defined as

$$\dot{f}_N=A\dot{\varepsilon}_p \quad (8)$$

with the function:

$$A=\frac{f_N}{S_N\sqrt{2\pi}}\exp\left(-\frac{1}{2}\left(\frac{\varepsilon_p-\varepsilon_N}{S_N}\right)^2\right) \quad (9)$$

where f_N is the void volume fraction of nucleating particles, ε_N is the mean nucleation strain, S_N is the standard deviation of nucleation strain, and $\dot{\varepsilon}_p$ is the equivalent plastic strain.

Eight parameters need to be determined for fracture failure analysis using the GTN model, which are yield function coefficients (q_1 and q_2), void nucleation parameters (f_0, ε_N, f_N and S_N) and void volume fraction (f_c and f_F). The parameters q_1 and q_2 depend strongly on both the strain hardening (n) and the ratio of yield strength to Young's modulus (YS/E) [37]. The values for q_1 and q_2 of the selected three samples were then solved based on the parameters as shown in Table 2. BACHA et al [31] and THUILLIER et al [38] have confirmed that the initial void nonzero value did not lead to significant changes in the results. Moreover, the initial void which was defined as 0 also obtained good results. So the value of f_0 was set as 0 in this study. Void nucleation mainly occurs during the necking process. Therefore, the mean nucleation strain ε_N was considered to be equal to the strain when necking appeared [39]. The ε_N values of the pre-aging, under-aging, peak-aging and over-aging treatment alloys were 0.148, 0.129, 0.122 and 0.105 respectively corresponding to the true strain in UTS. The nucleation rate function parameter S_N and the void volume fraction parameters (f_N, f_c, f_F) cannot be obtained directly neither by microstructure observation nor through tensile test [40,41]. In this case, the LS-OPT software was used to optimize the parameter values, and the minimum mean square

error fitting between the test curve and the simulation curve was taken as the optimization objective. The obtained GTN damage model parameters are listed in Table 4. As shown in Fig. 10, both the simulated force−displacement and fracture response agree well with the experimental results.

Table 4 GTN damage model parameters of 7003 aluminum alloys under different aging treatments

Aging treatment	q_1	q_2	f_0	ε_N	S_N	f_N	f_c	f_F
Pre-aging	1.5	1.0	0	0.148	0.3	0.08	0.004	0.25
Under-aging	1.5	1.0	0	0.129	0.3	0.078	0.002	0.32
Peak-aging	1.5	1.0	0	0.122	0.3	0.06	0.004	0.2
Over-aging	1.5	1.0	0	0.105	0.3	0.035	0.0053	0.15

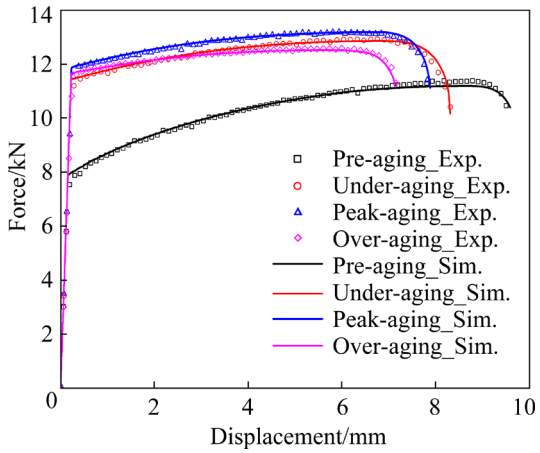

Fig. 10 Comparison between experimental and simulated force−displacement curves

3.3 Bending collapse and energy absorption of beams

3.3.1 FE model of three-point bending test

Figure 11 shows the FE model for the three-point bending test. As the influence of the transition filet characteristics of extruded profiles on the bending performance of the beam cannot be ignored, hexahedral solid elements are used in the large deformation area with a length of 200 mm in the middle of the beam. The element size is 0.75 mm, which is consistent with that of the uniaxial tension specimen. The Belytschko−Tsay shell element with the size of 3.0 mm is applied on both sides of the beam to improve the calculation efficiency. Five integration points are considered throughout the thickness of the shell element. Different types of elements are connected with rigid body elements. The SHS constitutive equation and GTN damage model are applied to simulating the bending collapse and fracture behavior of beams with MAT_GURSON_JC software. The punch and supports are considered rigid bodies with MAT_RIGID software. The "surface-to-surface" contact algorithm is considered among the punch, supports and beams. The "automatic single surface" contact is used to prescribe the beams to prevent interpenetration during bending collapse. The value of the contact friction coefficient is set as 0.2.

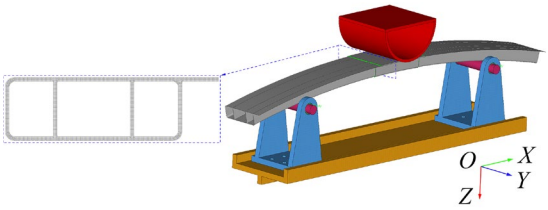

Fig. 11 FE model for three-point bending test

3.3.2 Bending collapse and energy absorption of 7003 aluminum alloy beams

Figure 12 depicts the experimental and simulated three-point bending load−displacement curves of the beams, as well as the deformation modes and cracking of beams at several typical instances. The whole bending process can be divided into three stages: elastic stage *OA*, pressure-holding stage *AB*, and unstable stage *BC*. The peak force and energy absorption characteristics of 7003 alloy beams under different aging conditions exhibited distinct variations, as illustrated in Fig. 13. During the elastic stage, the deformation of the beam is primarily a slight depression on the upper surface of the cavity, while the four stiffeners of the beam do not undergo any plastic deformation. When loading enters the pressure holding stage, the bearing capacity of the pre-aged beam increases gradually, while that of the under-aged beam decreases slowly. Figure 14(a) depicts the variation of middle stiffener distance with three-point bending deformation. With the increase of bending displacement, the distance increases slowly at first, and then increases rapidly after reaching a certain point. The turning point of the pre-aged beam is obviously later than that of the under-aged beam. This indicates that the pre-aged beam has a strong ability to resist structural instability in the pressure-holding stage [42]. The equivalent plastic strain history of the buckling point of stiffeners is extracted

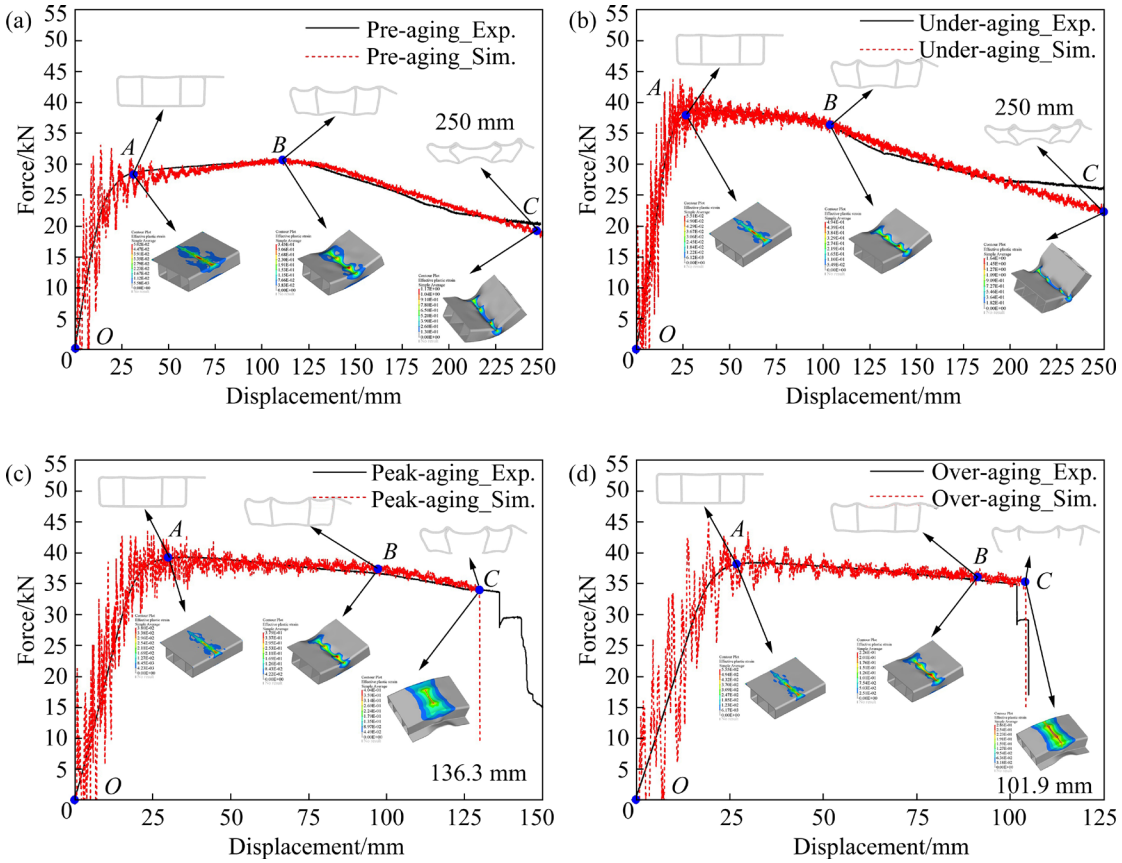

Fig. 12 Comparison of experimental and simulated force−displacement curves and cross-sectional evolution of beams under different aging treatments during three-point bending test: (a) Pre-aging; (b) Under-aging; (c) Peak-aging; (d) Over-aging

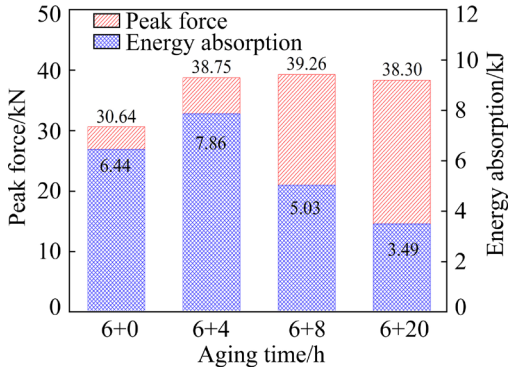

Fig. 13 Peak force and energy absorption of 7003 aluminum alloy beams under different aging treatments

from the finite element model and plotted in Fig. 14(b). It can be seen that the equivalent plastic strain at the buckling point varies between 0 and 0.2 in the pressure-holding stage. Within this range, the strain hardening rate of the pre-aged beam is significantly higher than that of the under-aged beam (Fig. 9). The strength improvement of the beam induced by strain hardening of the material is greater than the structural strength reduction induced by the deformation of the cavity. This induces a continuous increase in the bearing capacity of the pre-aged beam during the pressure-retaining stage. When the displacement exceeds the instability point *B*, the bearing capacity of the beam continues to decline. When the loading displacement reaches 250 mm, no fracture was observed in the pre-aged and under-aged beams during three-point bending test [43].

The tensile stress on the bottom surface of the beam is the primary factor inducing beam cracking during three-point bending test. Due to the low strain hardening rate and strain extension capacity of the peak-aged and over-aged beams, strain concentration is easy to appear on the lower surface of the middle cavity of the beam, leading to the initiation and propagation of cracks. The stress triaxiality and equivalent plastic strain at Point *P*1 under different aging treatments are shown in Fig. 15(a). The initial stress triaxiality of the beams at *P*1 is about 0.4. During the three-point bending process, *P*1 is mainly subjected to tension

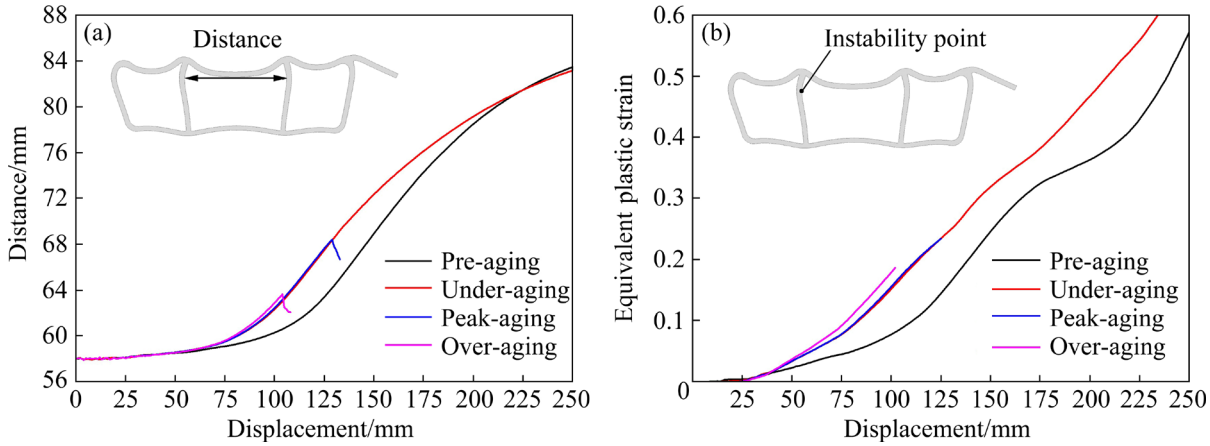

Fig. 14 Distance and instability point variation patterns of stiffeners during three-point bending process: (a) Distance−displacement curves of two middle stiffeners; (b) Equivalent plastic strain−displacement curves of instability point

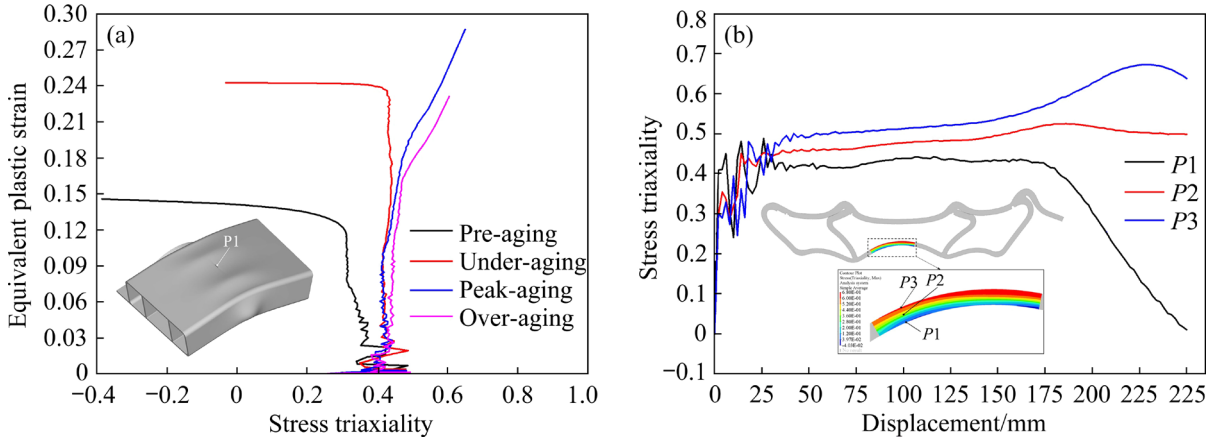

Fig. 15 Stress−strain curves of 7073 aluminum alloy beams under different aging treatments: (a) Equivalent plastic strain and stress triaxiality curves; (b) Stress triaxiality and displacement curves of under-aged beam

deformation with positive stress triaxiality levels for peak-aged and over-aged beams. However, the stress triaxiality of the pre-aged and under-aged beams transforms to be negative in the late deformation stage when the equivalent plastic strain exceeds 0.12 and 0.22, respectively, as shown in Fig. 15(a). Figure 15(b) shows the stress triaxiality variations at the selected three points $P1$−$P3$ during three-point bending of the under-aged beam. The stress triaxiality at $P2$ and $P3$ is higher than that at $P1$. The stress triaxiality at $P2$ and $P3$ varies from 0.45 to 0.66 (equi-biaxial tension), while at $P1$ it decreases drastically from 0.43 to 0 (pure shear). Figure 16 shows the comparison of the simulated and experimental deformation patterns of the beams. The large plastic deformation and fracture behaviors of the beams under different aging treatments are predicted by the established FE model.

4 Conclusions

(1) With the increase of aging time, the precipitates of 7003 aluminum alloy shift from GP II zones to η' phase. The YS and UTS increase during the pre-aging and under-aging stages. After peak aging, the strength decreases due to the coarsening of the η' phase. The continuous decrease of elongation with increasing aging time is caused by the coarsening of precipitates accompanied with the increase of the strength difference between the grain and grain boundary.

(2) The three-point bending collapse and cracking behaviors of the beams are accurately predicted by the SHS constitutive equation and GTN damage model. The peak force of three-point bending is positively related to the strength. The bearing capacity of the pre-aged beam increases

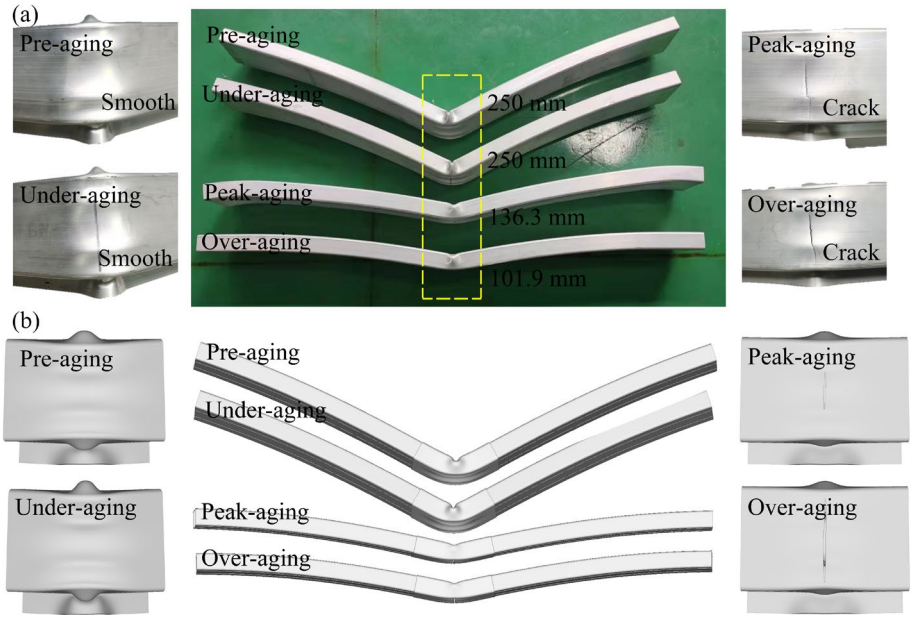

Fig. 16 Comparison between experimental and simulated results of three-point bending tests for 7073 aluminum alloy beams: (a) Experimental results; (b) Simulated results

continuously due to the high strain hardening rate of the alloy. While the bearing capacity of the other three beams shows a downward trend.

(3) When the beam bends to the set displacement of 250 mm, no crack exhibits on the pre-aged and under-aged beams. While the peak-aged and over-aged beams fracture at the displacement of 136.3 and 101.9 mm, respectively. Bending cracking is determined by the evolution of stress state. The stress triaxiality of pre-aged and under-aged beams at the corresponding positions evolves from 0.4 to negative value, and cracking is effectively restrained.

(4) The under-aged beam has the highest energy absorption of 7.86 kJ, and also has a higher peak load of 38.75 kN. This study provides valuable guidance for the manufacture of bumper beams that feature high bending stiffness, crack resistance, and energy absorption capabilities.

CRediT authorship contribution statement

Cong-chang XU: Conceptualization, Investigation, Writing − Original draft; **Han-lin XIANG:** Conceptualization, Supervision, Funding acquisition, Writing − Review and editing; **Teng ZHAN:** Formal analysis, Writing − Review and editing; **Peng-cheng GUO:** Formal analysis, Review and editing; **Luo-xing LI:** Formal analysis, Supervision, Funding acquisition, Writing − Review and editing.

Declaration of competing interest

The authors declare that they have no known competing financial interests or personal relationships that could have appeared to influence the work reported in this paper.

Data availability

Data will be made available on request.

Acknowledgments

This research was financially supported by the National Natural Science Foundation of China (Nos. 52272362, U20A20275) and the Technology Innovation and Application Development Special Key Project of Chongqing City, China (No. CSTB2022TIAD-KPX0035).

References

[1] DAVOODI M M, SAPUAN S M, AIDY A, ABU OSMAN N A, OSHKOUR A A, WAN ABAS W A B. Development process of new bumper beam for passenger car: A review [J]. Materials & Design, 2012, 40: 304−313.

[2] LI Zhi-gang, YANG Hai-feng, ZHANG Zhao-sheng, SUN Ye, HAN Zhi-tong, WEI Ji-fei. Crashworthiness of extruded magnesium thin-walled square tubes [J]. Transactions of Nonferrous Metals Society of China, 2019, 29: 1223−1232.

[3] LONG Jian, ZHANG Lin-jie, ZHU Lei, ZHANG Li-xu, WU Jun, ZHUANG Ming-xiang. Comparison of low-cycle fatigue properties of two kinds of high energy beam welded joints of TC4 alloy [J]. Transactions of Nonferrous Metals Society of China, 2023, 33: 3376−3386.

[4] SKOKKUL A, MLANGSET H, SHOPPERSTAD O, OGLADEM O. Offset impact behavior of bumper beam-longitudinal systems: Numerical simulations [J]. International Journal of Crashworthiness, 2006, 11: 299−316.

[5] DÍAZ-ÁLVAREZ A, FENG C, SANTIUSTE C. Energy absorption and residual bending behavior of biocomposites bumper beams [J]. Composite Structures, 2020, 245: 112343.

[6] BAI Jian-tao, MENG Guang-wei, WU Hong, ZUO Wen-jie. Bending collapse of dual rectangle thin-walled tubes for conceptual design [J]. Thin-Walled Structures, 2019, 135: 185−195.

[7] KIM T H, REID S R. Bending collapse of thin-walled rectangular section columns [J]. Computers & Structures, 2001, 79: 1897−1911.

[8] QIAN Ling-yun, PAREDES M, WIERZBICKI T, SPARRER Y, FEUERSTEIN M, ZENG Pan, FANG Gang. Experimental and numerical study on shear-punch test of 6060 T6 extruded aluminum profile [J]. International Journal of Mechanical Sciences, 2016, 118: 205−218.

[9] HIRSCH J G. Recent development in aluminium for automotive applications [J]. Transactions of Nonferrous Metals Society of China, 2014, 24: 1995−2002.

[10] MIKLOS T, IMRE C. Comparative study of the application of steels and aluminium in lightweight production of automotive parts [J]. International Journal of Lightweight Materials and Manufacture, 2018, 1: 229−238.

[11] SUN Guang-yong, WANG Xue-song, FANG Jian-guang, PANG Tong, LI Qing. Parallelized optimization design of bumper systems under multiple low-speed impact loads [J]. Thin-Walled Structures, 2021, 167: 108197.

[12] BILSTON D, RUAN D, CANDIDO A, DURANDET Y. Parametric study of the cross-section shape of aluminium tubes in dynamic three-point bending [J]. Thin-Walled Structures, 2019, 136: 315−322.

[13] DU Zhan-peng, DUAN Li-bin, CHENG Ai-guo, XU Zhi-dan, ZHANG Guang-ya. Theoretical prediction and crashworthiness optimization of thin-walled structures with single-box multi-cell section under three-point bending loading [J]. International Journal of Mechanical Sciences, 2019, 157: 703−714.

[14] HUANG Zhi-xin, ZHANG Xiong, FU Xin-rong. On the bending force response of thin-walled beams under transverse loading [J]. Thin-Walled Structures, 2020, 154: 106807.

[15] WANG Zong, LI Zhen-huan, ZHANG Xiong. Bending resistance of thin-walled multi-cell square tubes [J]. Thin-Walled Structures, 2016, 107: 287−299.

[16] WANG Zong, ZHANG Xiong, LI Zhen-huan. Bending collapse of multi-cell tubes [J]. International Journal of Mechanical Sciences, 2017, 134: 445−459.

[17] RAO S, SRINIVASA, VISWATEJ K, ADINARAYANA S. Design and sensitivities analysis on automotive bumper beam subjected to low velocity impact [J]. International Journal of Engineering Trends and Technology, 2016, 37: 110−121.

[18] JUAN Yong-fei, NIU Guo-shuai, YANG Yang, XU Zi-han, YANG Jian, TANG Wen-qi, JIANG Hai-tao, HAN Yan-feng, DAI Yong-bing, ZHANG Jiao, SUN Bao-de. Accelerated design of Al−Zn−Mg−Cu alloys via machine learning [J]. Transactions of Nonferrous Metals Society of China, 2024, 34: 709−723.

[19] FAN Cai-he, LI Yi-hui, WU Qin, OU Ling, HU Ze-yi, NI Yu-meng, YANG Jian-jun. Effect of cold rolling deformation on microstructure evolution and mechanical properties of spray formed Al−Zn−Mg−Cu−Cr alloys [J]. Transactions of Nonferrous Metals Society of China, 2024, 34: 2442−2454.

[20] SERT A, GURGEN S, CELIK O N, KUSHAN M C. Effect of heat treatment on the bending behavior of aluminum alloy tubes [J]. Journal of Mechanical Science and Technology, 2017, 31: 5273−5278.

[21] BERG L K, GJØNNES J, HANSEN V, LI X Z, KNUTSON-WEDEL M, WATERLOO G, SCHRYVERS D, WALLENBERG L R. GP-zones in Al−Zn−Mg alloys and their role in artificial aging [J]. Acta Materialia, 2001, 49: 3443−3451.

[22] CHEMINGUI M, KHITOUNI M, JOZWIAK K, MESMACQUE G, KOLSI A. Characterization of the mechanical properties changes in an Al−Zn−Mg alloy after a two-step aging treatment at 70 °C and 135 °C [J]. Materials & Design, 2010, 31: 3134−3139.

[23] LI Bo, PAN Qing-lin, CHEN Cong-ping, WU Hai-hua, YIN Zhi-min. Effects of solution treatment on microstructural and mechanical properties of Al−Zn−Mg alloy by microalloying with Sc and Zr [J]. Journal of Alloys and Compounds, 2016, 664: 553−564.

[24] WEN Kai, FAN Yun-qiang, WANG Guo-jun, JIN Long-bin, LI Xi-wu, LI Zhi-hui, ZHANG Yong-an, XIONG Bai-qing. Aging behavior and precipitate characterization of a high Zn-containing Al−Zn−Mg−Cu alloy with various tempers [J]. Materials & Design, 2016, 101: 16−23.

[25] ZHANG Zhen, DENG Yun-lai, YE Ling-ying, SUN Lin, XIAO Tao, GUO Xiao-bin. Effect of multi-stage aging treatments on the precipitation and mechanical properties of Al−Zn−Mg alloys [J]. Materials Science and Engineering: A, 2020, 785: 139394.

[26] LI Ji-feng, BIRBILIS N, LI Cun-xi, JIA Zhi-qiang, CAI Bin, ZHENG Zhi-qiang. Influence of retrogression temperature and time on the mechanical properties and exfoliation corrosion behavior of aluminium alloy AA7150 [J]. Materials Characterization, 2009, 60: 1334−1341.

[27] HUANG Xing, PAN Qing-lin, LI Bo, LIU Zhi-ming, HUANG Zhi-qi, YIN Zhi-min. Microstructure, mechanical properties and stress corrosion cracking of Al−Zn−Mg−Zr alloy sheet with trace amount of Sc [J]. Journal of Alloys and Compounds, 2015, 650: 805−820.

[28] FOMIN E V, MAYER A E, KRASNIKOV V S. Prediction of shear strength of cluster-strengthened aluminum with multi-scale approach describing transition from cutting to bypass of precipitates by dislocations [J]. International Journal of Plasticity, 2021, 7088: 103095.

[29] SHENG Xiao-fei, HE Cun-xiao, CHENG Ya-juan, RAO Xiao-xiao, HE Guo-ai. New method and mechanism for quickly obtaining quenching sensitivity temperature range of 7055 aluminum alloy [J]. Transactions of Nonferrous Metals Society of China, 2023, 33: 36−45.

[30] YANG Xian-wen, YE Ling-ying, ZHANG Yong, CHENG Quan-shi. Effect of interrupted aging on mechanical

properties and corrosion resistance of 7A75 aluminum alloy [J]. Transactions of Nonferrous Metals Society of China, 2024, 34: 2415−2430.
[31] BACHA A, DANIEL D, KLOCKER H. On the determination of true stress triaxiality in sheet metal [J]. Journal of Materials Processing Technology, 2007, 184: 272−287.
[32] ZHU Lu, LIU Wei-qiang, FANG Hai, CHEN Ji-ye, ZHUANG Yong, HAN Juan. Design and simulation of innovative foam-filled lattice composite bumper system for bridge protection in ship collisions [J]. Composites Part B: Engineering, 2019, 157: 24−35.
[33] GURSON K, ANDER L. Continuum theory of ductile rupture by void nucleation and growth: Part I—Yield criteria and flow rules for porous ductile media [J]. Journal of Engineering Materials and Technology, 1977, 99: 2−15.
[34] TVERGAARD V. Influence of voids on shear band instabilities under plane strain conditions [J]. International Journal of Fracture, 1981, 17: 389−407.
[35] TVERGAARD V. Influence of void nucleation on ductile shear fracture at a free surface [J]. Journal of the Mechanics and Physics of Solids, 1982, 30: 399−425.
[36] LI Heng, FU Ma-wei, LU Jiang, YANG He. Ductile fracture: Experiments and computations [J]. International Journal of Plasticity, 2011, 27: 147−180.
[37] FALESKOG J, GAO Xiao-sheng, SHIH C. Cell model for nonlinear fracture analysis—I. Micromechanics calibration [J]. International Journal of Fracture, 1998, 89: 355−373.
[38] THUILLIER S, LE MAOÛT L, MANACH P Y. Influence of ductile damage on the bending behaviour of aluminium alloy thin sheets [J]. Materials & Design, 2011, 32: 2049−2057.
[39] YAN Yu-xi, SUN Quan, CHEN Jian-jun, PAN Hong-liang. The initiation and propagation of edge cracks of silicon steel during tandem cold rolling process based on the Gurson–Tvergaard–Needleman damage model [J]. Journal of Materials Processing Technology, 2013, 213: 598−605.
[40] CHHIBBER R, ARORA N, GUPTA S R, DUTTA B K. Estimation of Gurson material parameters in bimetallic weldments for the nuclear reactor heat transport piping system [J]. Proceedings of the Institution of Mechanical Engineers (Part C): Journal of Mechanical Engineering Science, 2008, 222: 2331−2349.
[41] ZHANG Zhi-Lin, THAULOW C, ODEGARD J. A complete Gurson model approach for ductile fracture [J]. Engineering Fracture Mechanics, 2000, 67: 155−168.
[42] ESTRADA Q R, SZWEDOWICZ D, TRAN T, RODRIGUEZ M A, ELIAS E M, GÔMEZVARGAS O A, PARTIDA O G. Bending crashworthiness of elliptical tubes with different aspect ratio and stiffeners [J]. The International Journal of Advanced Manufacturing Technology, 2022, 120: 6661−6680.
[43] WANG Han, ZHANG Hai-ming, CUI Zhen-shan, CHEN Zhe, CHEN Dong. Ductile fracture behavior of in situ TiB_2 particle reinforced 7075 aluminum matrix composite in various stress states [J]. Transactions of Nonferrous Metals Society of China, 2023, 33: 2272−2286.

时效处理对 7003 铝合金前防撞横梁弯曲坍塌行为及吸能性能的影响

徐从昌[1,2]，向瀚林[1,2]，詹 腾[1,2]，郭鹏程[2]，李落星[1,2]

1. 湖南大学 机械与运载工程学院，长沙 410082；
2. 湖南大学 重庆研究院，重庆 400044

摘 要：通过三点弯曲试验研究了 7003 铝合金防撞横梁在 4 种时效状态(预时效、欠时效、峰时效和过时效)下的弯曲坍塌行为与吸能性能。利用扫描电子显微镜和透射电子显微镜对经时效处理后铝合金的显微组织进行了表征。基于 Swift−Hockett−Sherby 本构模型与 Gurson−Tvergaard−Needleman 损伤模型的耦合分析，准确预测了 7003 铝合金在单轴拉伸和三点弯曲条件下的塑性响应与断裂行为。结果表明，横梁的峰值弯曲力与不同时效状态 7003 铝合金的强度呈正相关，而应力三轴性是决定横梁开裂失效的关键因素。预时效与欠时效横梁在达到 250 mm 位移前均未发生开裂，这归因于横梁底部表面应力从拉应力向压应力的转变。其中，欠时效横梁表现出最优的吸能性能 (7.86 kJ)，同时具有较高的峰值承载力 (38.75 kN)。

关键词：7003 铝合金横梁；时效处理；三点弯曲试验；弯曲塌陷；吸能性能

(Edited by Wei-ping CHEN)